ACS APPLIED MATERIALS & INTERFACES

www.acsami.org

Research Article

Multiwavelength-Responsive Plasticity in a Bias-Free Perovskite Synaptic Device for Neuromorphic Vision

Juan Gao, Qin Gao,* Jiangshun Huang, Xueli Geng, Pengzhan Li, Yihang Liu, Qiaofeng Yang, Hao Zhang, Mei Wang, Zhisong Xiao, Paul K. Chu, Ruifeng Lu, and Anping Huang*

Cite This: *ACS Appl. Mater. Interfaces* 2025, 17, 48465−48473

Read Online

ACCESS | Metrics & More | Article Recommendations | Supporting Information

ABSTRACT: Low-power and color-sensitive neuromorphic vision systems are critical to the next generation of intelligent devices. Here, we report a coral-inspired, lead-free synaptic device based on $Cs_3Bi_2Br_9$ perovskite nanocrystals prepared by centrifugal casting into a porous thin film. The device exhibits wavelength-dependent plasticity under 405, 520, and 635 nm illumination without an external bias. By modulating the light wavelength and intensity, short-term and long-term synaptic plasticity are achieved to mimic excitatory, inhibitory, and saturating biological responses. Structural and spectroscopic analyses reveal that bromine vacancies play a key role in the dynamic modulation of carrier transport and plasticity evolution. The efficient preprocessing of RGB visual information significantly enhances recognition accuracy in artificial neural network devices. This wavelength-specific modulation of synaptic plasticity, a novel approach for color image preprocessing and recognition, is very promising for the advancement of neuromorphic systems.

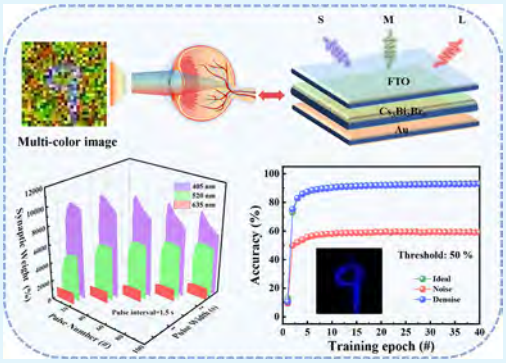

KEYWORDS: *synaptic plasticity, photoelectric property, coral-like perovskite, tunable; neurocomputing*

INTRODUCTION

The advancement of embodied intelligence is accelerating the demand for neuromorphic visual systems (NVSs) that emulate human visual processing.[1−3] Unlike traditional systems, NVSs merge sensing, processing, and memory to allow fast and efficient perception, a key feature for smart agents in changing environments.[4−6] However, the development of such systems faces significant challenges, particularly in achieving low-power operation, multiwavelength sensitivity, and dynamic synaptic plasticity, which are key features that underpin biological vision.[7−9] Current optoelectronic synapses often exhibit mutually exclusive short-term plasticity (STP) and long-term plasticity (LTP), require external voltage biases, and lack color-discriminative capabilities.[10,11] These limitations restrict their ability to emulate adaptive learning and parallel processing of biological visual pathways.

In recent years, research on optically controlled synaptic devices has partially alleviated the aforementioned limitations. Several studies have demonstrated wavelength-dependent, light-induced nonvolatile excitatory and inhibitory responses,[12,13] indicating that spectral modulation offers a feasible approach to construct color-sensitive neuromorphic devices. For instance, materials such as MoS_2 and ZnO exhibit excitatory or inhibitory synaptic behaviors under different illumination wavelengths, with some systems even achieving reversible switching of synaptic states via optical stimulation.[14−16] However, most of these devices still rely on electrical assistance or specific material architectures, thus limiting their potential in achieving self-powered operation, enhanced controllability, and broad applicability.[7,9,17−19] Halide perovskites offer tunable bandgaps, high defect tolerance, and strong light-matter interactions, enabling efficient carrier transport and defect-mediated plasticity.[18,20,21] In particular, lead-based perovskites like $MAPbI_3$ show promising synaptic behaviors, but toxicity and instability limit their use.[22,23]

Inspired by coral photobiology, which achieves efficient light harvesting through hierarchical pore architectures and ion migration-mediated spectral tuning,[24−26] we propose a multiwavelength-dependent synaptic device based on $Cs_3Bi_2Br_9$ (CBB) perovskite. This device, composed of CBB perovskite nanocrystals (PNCs) fabricated using a centrifugal casting method, features a stack structure of Au/CBB/FTO. It shows wavelength-tunable synaptic plasticity across three distinct wavelengths—405, 520, and 635 nm—without the need for biasing. The mechanism of this wavelength-dependent behavior is rooted in the unique coral-like structure of CBB, which dynamically regulates light scattering, absorption, and

Received: May 15, 2025
Revised: July 29, 2025
Accepted: August 8, 2025
Published: August 14, 2025

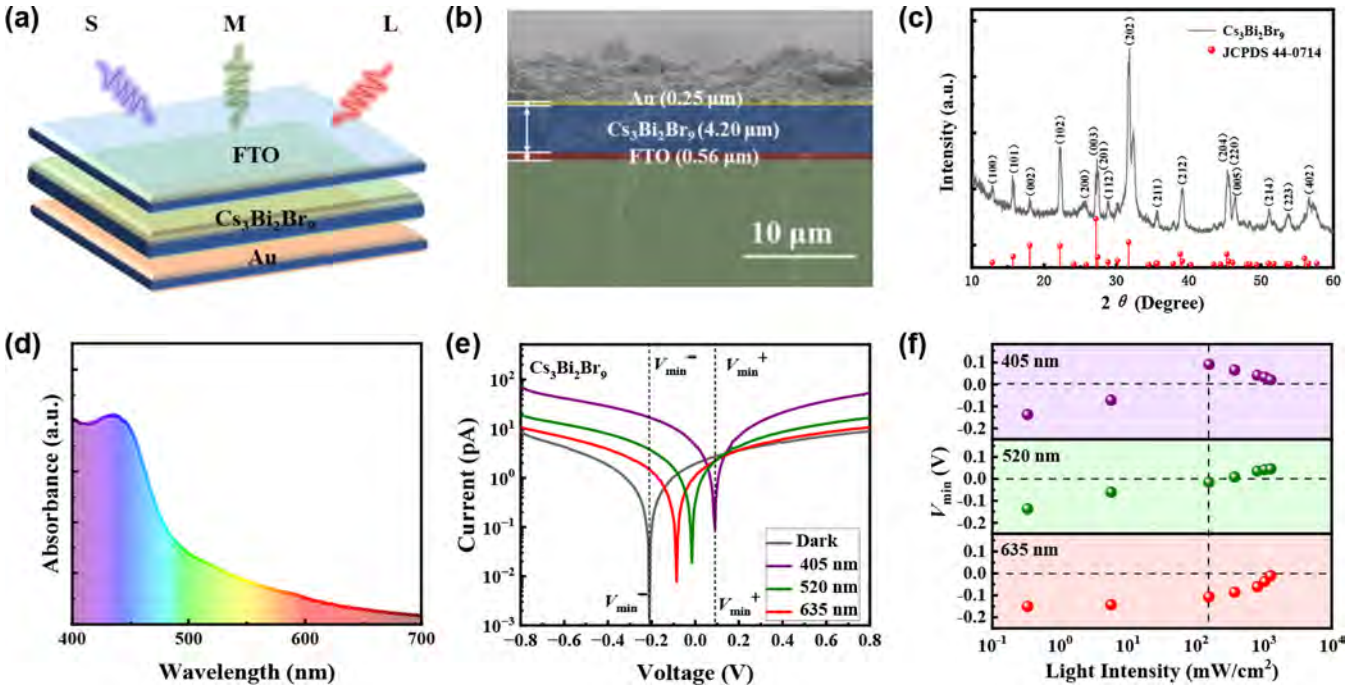

Figure 1. (a) Schematic diagram of the Au/CBB/FTO synaptic device; (b) cross-sectional SEM images of the device; (c) XRD patterns of the CBB PNCs; (d) absorption spectra of the CBB PNCs; (e) $I-V$ curves of the device under different wavelengths (405, 520, and 635 nm); (f) the relationship between V_{min} at different wavelengths and light intensity.

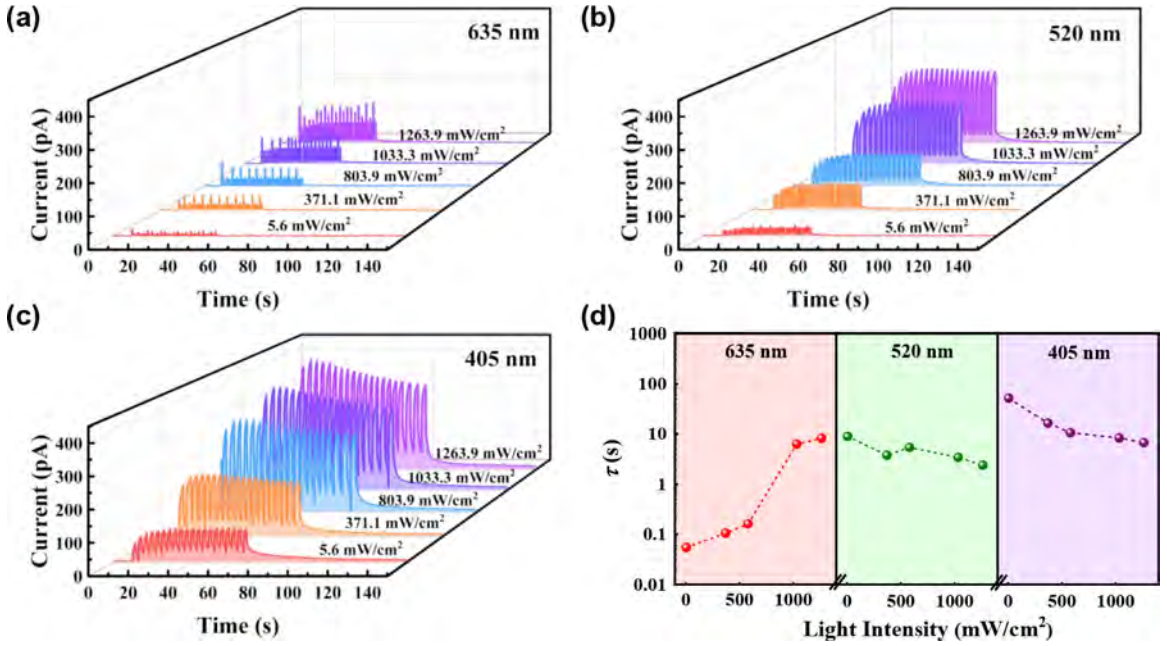

Figure 2. Optical pulse response characteristics at different optical power densities (5.6 mW/cm^2, 371.1 mW/cm^2, 803.9 mW/cm^2, 1033.3 mW/cm^2,1263.9 mW/cm^2); (a) 635 nm, (b) 520 nm, and (c) 405 nm wavelengths; (d) relationship between decay time, light intensity, and wavelength.

reflection to optimize the response under varying lighting conditions. The results, which reveal wavelength-coded photoinhibition/enhancement coexistence, establish a generalizable platform for energy-efficient, color-aware neuromorphic systems.

RESULTS AND DISCUSSION

The bionic synaptic device consists of Au/CBB/FTO, as shown in Figure 1a, where light is incident on the FTO side of the transparent electrode. The cross-sectional SEM diagram of the device in Figure 1b shows that the thickness of the CBB layer is about 4.2 μm. The corresponding EDS elemental maps are shown in Figure S1. Figure 1c shows the X-ray diffraction (XRD) patterns of the CBB perovskite. The diffraction peaks at 12.8°, 15.7°, 18.0°, 22.2°, 27.2°, 31.7°, and 45.2° can be assigned to the (100), (101), (002), (102), (003), (202), and (204) planes, respectively. These peaks correspond to the standard diffraction pattern of CBB PNCs (JCPDS No. 44-0714, space group $P3m1$, $a = b = 0.796$ nm, $c = 0.984$ nm), confirming that the material has high crystallinity and exhibits

https://doi.org/10.1021/acsami.5c09650
ACS Appl. Mater. Interfaces 2025, 17, 48465−48473

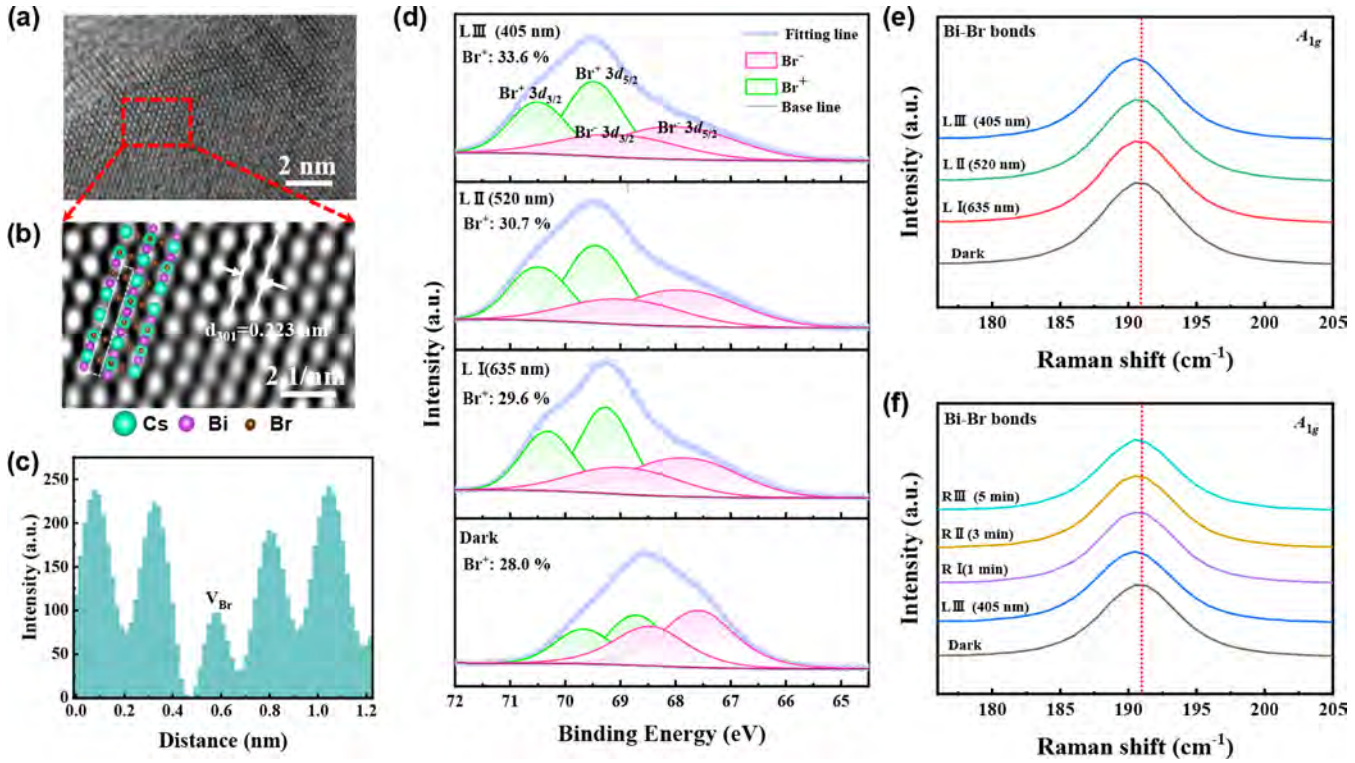

Figure 3. (a) HR-TEM images of CBB PNCs; (b) Partial enlarged drawing; (c) Lattice diffraction distribution image; (d) XPS Br 3*d* spectra of the CBB film irradiated under different light conditions; (e) A_{1g} displacement in the Raman spectra for different light conditions; (f) A_{1g} displacement in the Raman spectra for different recovery times after illumination.

trigonal symmetry.[27−29] The UV−visible optical absorption spectra of CBB perovskite, shown in Figure 1d, exhibit a light absorption range from 400 to 700 nm. The corresponding Tauc plot of the absorption spectra (Figure S2) reveals that CBB PNCs possess a direct bandgap of 2.58 eV, which is consistent with previous reports.[30,31] The *I*−*V* curves are acquired at different wavelengths (405, 520, and 635 nm) of light with an intensity of 155.6 mW/cm^2, as shown in Figure 1e. The device shows the highest response (~70 pA) to a 405 nm optical stimulus, which is consistent with the absorption feature of the CBB PNCs film. It is noted that the *I*−*V* curves exhibit a shift from zero under both dark and light conditions. The offset from zero in the dark is caused by the built-in electric field generated by the asymmetric electrode and the porous structure of the CBB PNCs thin film.[20,32,33] The photogenerated electric field, created by the photovoltaic effect, opposes the built-in electric field, causing the *I*−*V* zero offset to shift toward the positive voltage. As the wavelength decreases and the energy increases, the photogenerated electric field strengthens, causing a larger shift in the deviation point.

To further investigate the device response to optical signals, experiments were conducted for different wavelengths and light intensities, as shown in Figure S3, and the statistical analysis is presented in Figure 1f. As light intensity increases, the zero-offset point shifts toward the positive voltage, indicating that photogenerated electron−hole pairs accumulate near the interface to form a reverse electric field that weakens the built-in electric field. This leads to a positive shift of the zero-bias point, with the degree of shift increasing with light intensity. At 635 nm, the photon energy is below the bandgap of the perovskite, thereby exciting only shallow-level states and generating a limited number of carriers, resulting in the zero offset moving from −0.15 V to −0.01 V. At 520 nm, the photon energy is near the bandgap, generating abundant free carriers and activating interface states, which significantly weaken the built-in field and cause the zero-offset point to shift from −0.1 V to 0.05 V. At 405 nm, where the photon energy exceeds the bandgap, deep-level defect states are excited, and Br^- ion migration is triggered. At low light intensity, the zero-offset point shifts from −0.14 V to 0.09 V. At higher intensities, photoinduced Br^- migration leads to the formation of bromine vacancies (V_{Br}), which serve as defect centers to accelerate carrier recombination,[34] thereby reducing the photoinduced electric field and causing the intersection point to shift back to 0.02 V.

Figure 2a-c shows the optical pulse response of the device at 635 nm, 520 nm, and 405 nm, respectively. Five optical pulse sequences with different optical power densities (5.6 mW/cm^2, 371.1 mW/cm^2, 803.9 mW/cm^2, 1033.3 mW/cm^2, and 1263.9 mW/cm^2) are applied. The pulse train consists of 20 cycles, each with a 3 s duration (pulse width of 1.5 s, interval of 1.5 s). It is observed that shorter wavelengths produce larger optical pulse responses at the same optical power density, while higher optical intensities lead to greater responses at a fixed wavelength. When the incident wavelength is 635 nm and the optical intensity is below 803.9 mW/cm^2, as shown in Figure 2a, the photocurrent shows little change with the increase in pulse number. However, when the optical power density exceeds 803.9 mW/cm^2, the photocurrent increases as the pulse number rises. This behavior is analogous to excitatory synaptic activity in biological synapses, where a stronger stimulus leads to a higher amplitude response. When the incident wavelength is 520 nm and the optical power density is below 1033.3 mW/cm^2 [Figure 2b], the photo-

https://doi.org/10.1021/acsami.5c09650
ACS Appl. Mater. Interfaces 2025, 17, 48465−48473

current increases with the pulse number. However, when the optical power density exceeds 1033.3 mW/cm^2, the photocurrent plateaus and tends toward saturation, resembling biological synaptic saturation, in which further increases in stimulus intensity do not produce a higher amplitude response. At a wavelength of 405 nm and an optical power density below 371.1 mW/cm^2 (Figure 2c), the photocurrent increases with the pulse number. Beyond 371.1 mW/cm^2, the photocurrent decreases as the pulse number increases, mimicking the inhibitory synaptic behavior in biological systems, where stronger stimuli hyperpolarize the synaptic neuron, resulting in a lower amplitude response. The decay time, which refers to the time it takes for the photocurrent to decrease from 90% to 10% of its maximum value,[35] is calculated for light pulse sequences of different wavelengths and light intensities, as shown in Figure 2a-c. The results are presented in Figure 2d. The device exhibits transition characteristics of STP and LTP by varying the incident light wavelengths. At incident wavelengths of 635 nm and 520 nm, the photocurrent decay time is shorter, indicating STP. It gradually increases with higher light intensity. At 405 nm, the photocurrent decay time is longer, indicative of LTP behavior, and decreases with higher light intensity. The EPSC and PPF characteristics of the device are shown in Figures S4 and S5, respectively. The comparison with previously reported lead-free and lead-based perovskite nanocrystal devices is summarized in Tables S1 and S2, respectively. This device does not require a bias voltage and has properties comparable to those of other reported devices.

To clarify the transition behavior from STP to LTP under different lighting conditions, microscopic morphology characterization is performed, and the results are presented in Figure S6. The surface morphology of the CBB layer exhibits a hierarchical porous structure, as shown in Figure S6a, which is similar to the coral-like structure in Figure S6c. Figure S6b is the cross-sectional SEM image of the CBB layer, which is similar to that in Figure S6d. In nature, corals enhance light utilization through the dynamic regulation of their porous morphology and internal pigments under different lighting conditions (Figure S6e), consequently enabling efficient light energy absorption and self-protection.[24,25] Figure S7 shows the EDS results of Cs, Bi, and Br in the CBB film. Figure 3a shows the HR-TEM image of CBB PNCs, and Figure 3b is an enlarged view of the red box in Figure 3a. The interlayer spacing of ∼0.22 nm corresponds to the (301) crystal planes. The lattice diffraction intensity distribution of Br confirms the presence of V_{Br} in the CBB structure, with a significant intensity reduction, as shown in Figure 3c. In situ X-ray photoelectron spectroscopy (XPS) and Raman scattering are performed to analyze the change of V_{Br} under different illumination conditions, as shown in Figure 3d-f. Figure 3d presents the XPS results of Br^- $3d_{3/2}$, Br^- $3d_{5/2}$, Br^+ $3d_{3/2}$, and Br^+ $3d_{5/2}$ under different lighting conditions, specifically LI (635 nm), LII (520 nm), and LIII (405 nm) irradiation for 2 min, respectively.[36,37] The corresponding full spectrum of the CBB structure and the core-level spectra of Cs 3*d* and Bi 4*f* are shown in Figure S8a-c, respectively. The transition mechanism from STP to LTP is elucidated by analyzing the variation in the Br^+ content in the CBB structure under different illumination conditions. Under illumination at 635, 520, and 405 nm, the Br^+ concentrations are 29.6%, 30.7%, and 33.6%, respectively, which are notably higher than the 28% observed in the dark state. The lattice vibration dynamics of the CBB structure under different illumination conditions is investigated by Raman scattering. The vibration mode of Bi−Br bonds corresponds to two peaks of A_{1g} (190.78 cm^{-1}) and E_g (165.80 cm^{-1}).[38,39] Figure 3e,f shows the changes of the A_{1g} peak under dark and different illumination conditions [LI (635 nm), LII (520 nm), and LIII (405 nm) irradiation for 2 min], as well as different recovery times after 405 nm illumination (1, 3, and 5 min) respectively. The corresponding changes of E_g peaks are shown in Figure S9a,b. Compared to the dark condition, the characteristic peaks of A_{1g} and E_g shift toward lower wave numbers, as shown in Figures 3e and S9a. The following is the relationship described by the Raman shift formula:[40]

$$\omega = \frac{1}{2\pi c}\sqrt{\frac{k}{\mu}} \tag{1}$$

where ω is the Raman shift (cm^{-1}), c is the velocity of light, and μ is the effective mass. The Raman shift of the Bi−Br bond (E_g and A_{1g}) is attributed to the decreased force constant (k) of the Bi−Br bonds caused by the introduction of V_{Br}. The result further confirms the generation of V_{Br} during light irradiation, and a shorter wavelength leads to stronger light energy and increased V_{Br} generation. As the recovery time increases under the dark condition, the characteristic peaks of A_{1g} and E_g gradually shift toward higher wave numbers in Figures 3f and S9b, indicating that the generation of V_{Br} is reversible. Figure S10 shows the ultraviolet photoelectron spectroscopy (UPS) results and optical bandgap of Figure S2 to obtain the conduction band minimum and valence band maximum of the CBB layer. Figure S11 presents the energy band diagram of the CBB synaptic device under different illumination conditions. Upon excitation by a 635 nm laser, some electrons in the CBB film are excited from the valence band (VB) to the conduction band (CB) to generate photogenerated electrons and holes, which then transfer to the FTO and Au electrodes, respectively. In the Schottky junction formed between the perovskite layer and the metal electrode, the alignment of the Fermi levels gives rise to energy band bending at the interface, resulting in the formation of a depletion region with a width of H_1 on the semiconductor side, as illustrated in Figure S11b. With increasing incident photon energy, a large number of photogenerated electron−hole pairs are produced in the perovskite layer. Some of these carriers accumulate near the interface and are trapped in shallow defect states. This redistribution of charge modulates the local Schottky barrier height, leading to further band bending and a reduction in the depletion width to H_2, manifested as enhanced photocurrents and STP, as shown in Figure S11c. Upon further increasing the incident photon energy, intense illumination generates more photocarriers and simultaneously drives the migration of Br^- to form V_{Br}. These deep-level defects affect the capture and release dynamics of photogenerated carriers, giving rise to LTP.[41,42] Additionally, V_{Br} can act as nonradiative recombination centers to accelerate carrier recombination. As the illumination duration increases, the concentration of V_{Br} rises, leading to an initial enhancement followed by a gradual decay of the photocurrent due to recombination losses,[43,44] as shown in Figure S11d. This response, characterized by an initial increase and subsequent decrease of the photocurrent, resembles the light-enhanced energy effect in coral.[25]

About 80% of the information humans receive comes from the eyes. Different light energy stimuli regulate the ion channels of retinal photoreceptors, alter cell conductivity and neuronal potential, and affect synaptic plasticity to optimize

https://doi.org/10.1021/acsami.5c09650
ACS Appl. Mater. Interfaces 2025, 17, 48465−48473

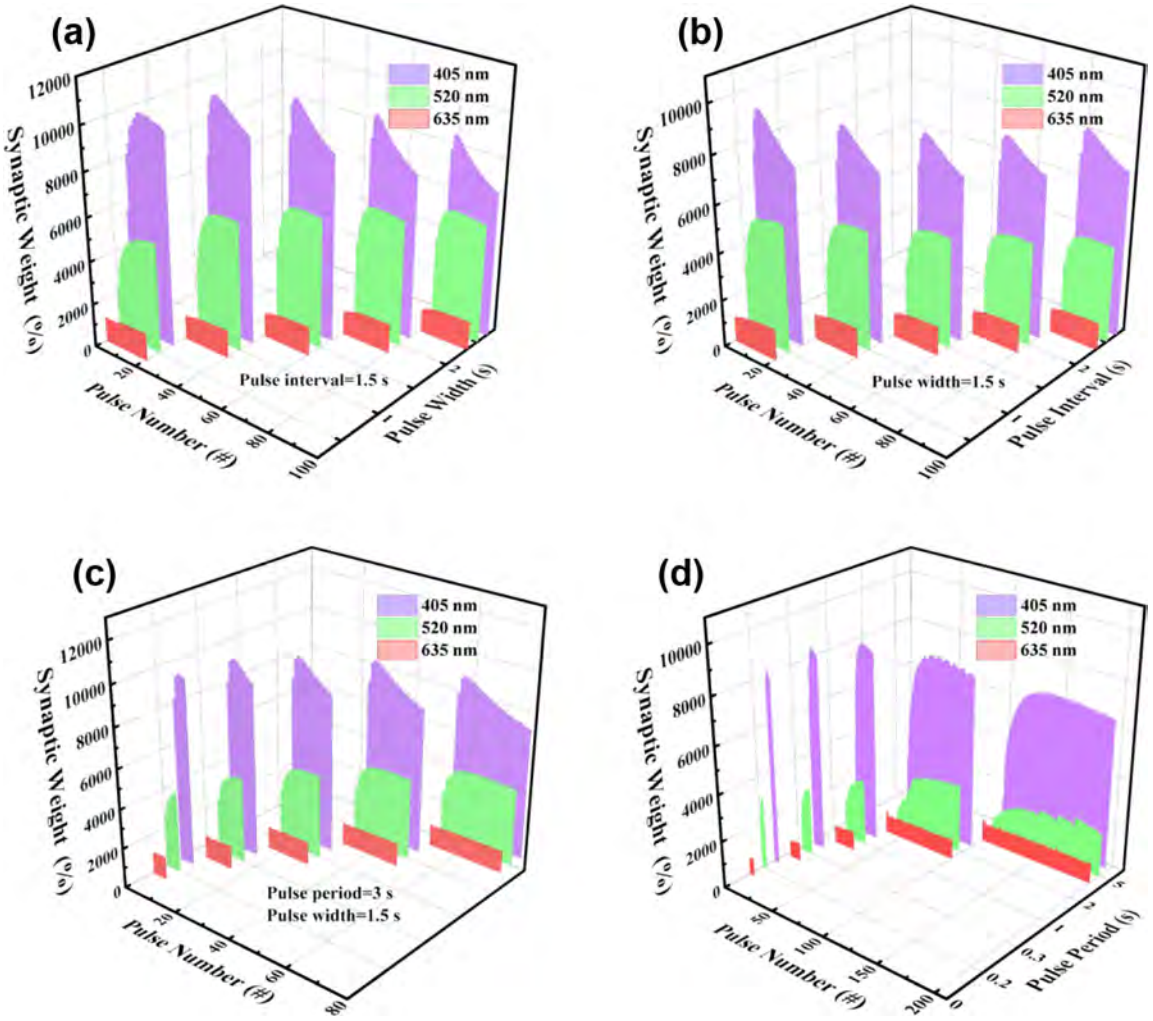

Figure 4. Synaptic plasticity modulation by varying (a) pulse width (0.5, 1, 1.5, 2, and 2.5 s); (b) pulse interval (0.5, 1, 1.5, 2, and 2.5 s); (c) pulse numbers (5, 10, 15, 20, and 25); and (d) pulse periods (0.2 s, 0.3 s, 1 s, 2 s, 3 s) for different wavelengths (405 nm, 520 nm, 635 nm).

visual signal transmission.[45] Synaptic plasticity, such as STP and LTP, is simulated by stimulation with different wavelengths (405, 520, and 635 nm). To mimic the dynamic regulation of the device, a series of light pulses with different pulse widths (0.5 s, 1 s, 1.5 s, 2 s, and 2.5 s), pulse intervals (0.5 s, 1 s, 1.5 s, 2 s, and 2.5 s), pulse numbers (5, 10, 15, 20, and 25), pulse periods (0.2 s, 0.3 s, 1 s, 2 s, and 3 s), and intensity of 803.9 mW/cm^2 are applied as external stimuli, as shown in Figure 4a–d. The synaptic weight increases as the incident wavelength decreases. Upon 635 nm laser stimulation, the synaptic weight gradually strengthens as the pulse width increases from 0.5 to 2.5 s. A larger pulse width generates more photogenerated carriers, which are trapped in defect states in the perovskite photosensitive layer and at electrode interfaces, resulting in photocurrent accumulation and enhanced synaptic weight. During 520 nm laser stimulation, the synaptic weight initially increases with pulse widths (0.5–2 s), but for pulse widths between 2 and 2.5 s, it decreases gradually. This behavior is attributed to the higher photon energy of 520 nm wavelength light compared to that of 635 nm and the concomitant increased carrier recombination or saturation effects. For the same optical power density and pulse width, 520 nm light produces significant bromine ion migrations in perovskites, generates ion vacancy defects as recombination centers for photogenerated carriers, and reduces the synaptic weight. Owing to the higher photon energy, 405 nm light produces a more pronounced effect. As the pulse width increases (0.5–2.5 s), the synaptic weight decreases gradually, as shown in Figure 4a. Upon illumination with 405, 520, and 635 nm light, the synaptic weight increases as the pulse intervals decrease, as shown in Figure 4b. Conversely, Figure 4c illustrates that the synaptic weight decreases with an increasing number of light pulses, demonstrating that the optoelectronic device exhibits pulse-number-dependent plasticity for different wavelengths. As shown in Figure 4d, the synaptic weight declines gradually with increasing pulse frequencies in the light pulse sequence. The variations in synaptic weights can be described by the following formula:[46]

$$W\% = \left[\frac{I_n - I_0}{I_0}\right] \times 100\% \tag{2}$$

where I_0 is the initial current value, and I_n (n = 1, 2, 3, ... 20) is the corresponding current value after stimulation.

Extracting effective information from complex environmental data is crucial.[47,48] Our device demonstrates wavelength-dependent synaptic plasticity, making it suitable for color image preprocessing. As shown in Figure 5a, the original color image is decomposed into its R, G, and B components using Python, with the normalized RGB values mapped to light

https://doi.org/10.1021/acsami.5c09650
ACS Appl. Mater. Interfaces 2025, 17, 48465–48473

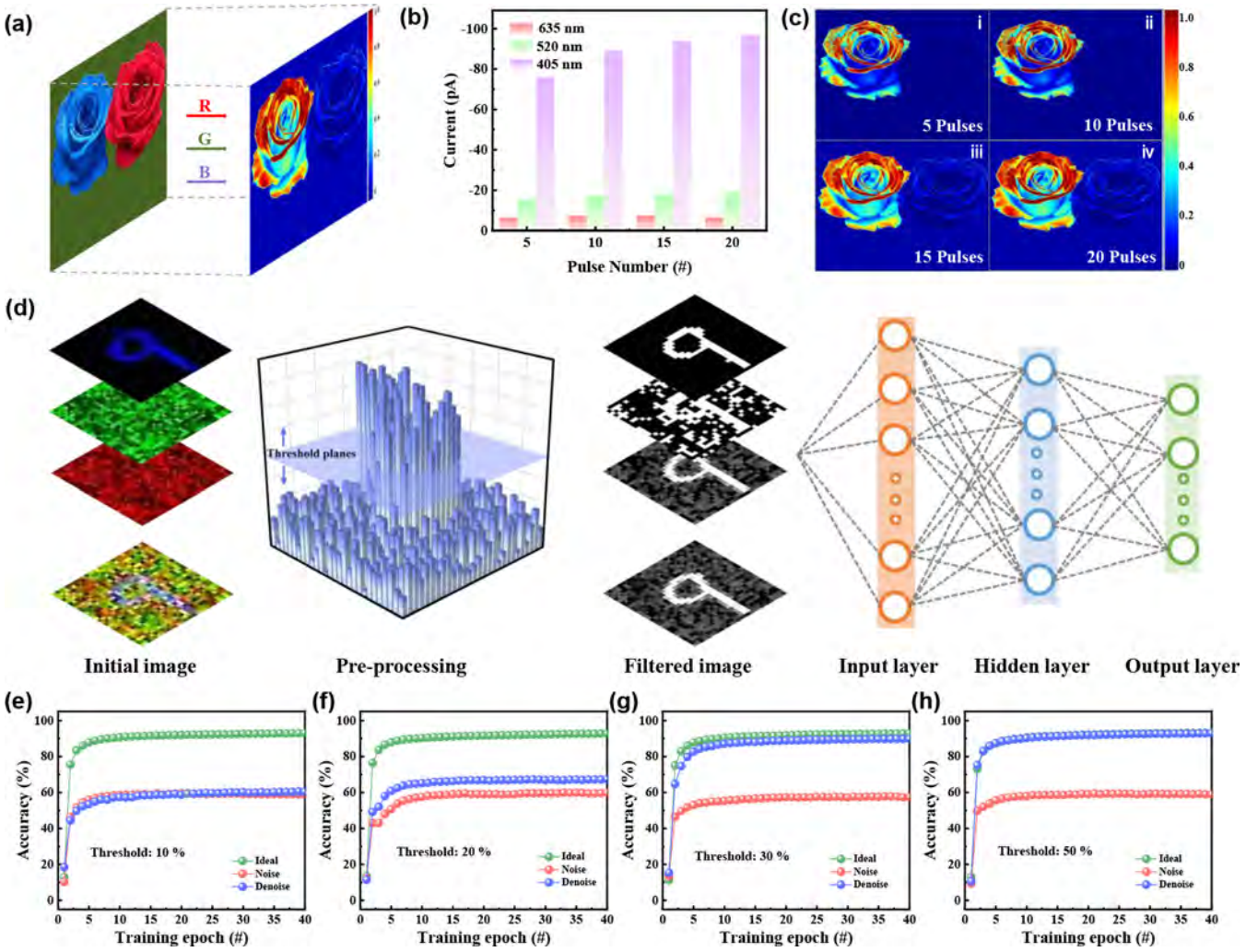

Figure 5. (a) Schematic image of encoding color information into the corresponding synaptic weight; (b) statistics of the channel photocurrent response as a function of pulse number under different wavelengths, namely red (red columns), green (green columns), and blue (blue columns) light pulses. The light intensity is 5.6 mW/cm^2 and the duration and interval are 0.5 s and 1.5 s, respectively; (c) differences between the blue and other features as the number of light pulses increases; (d) image preprocessing in neuromorphic vision systems and image recognition in artificial neural networks; comparison of recognition accuracy for different thresholds: (e) 10%; (f) 20%; (g) 30%; (h) 50%.

intensities corresponding to 635 nm (Red), 520 nm (Green), and 405 nm (Blue). Figure 5b presents the dependence of the photocurrents on the number of pulses at different wavelengths. The photocurrents are then used to reconstruct the output images. As illustrated in Figure 5c, increasing the number of pulses enhances the contrast between the blue feature and the other elements, making the blue object progressively clearer. An artificial vision system combining a neuromorphic vision device array with an artificial neural network (ANN) is designed and implemented. Experiments are conducted based on a modified version of the National Institute of Standards and Technology (MNIST) handwritten digit dataset, which is treated with Gaussian noise. The experiments are carried out in MATLAB 2023b. As shown in Figure 5d, the initial image is decomposed into three RGB images. The sampled RGB image is then passed to a 28 × 28 × 3 sensor array to convert the optical signal into a synaptic current, followed by summing the photocurrent from each channel to generate the output image. As shown in the second image in Figure 5d, the blue regions show higher currents. By adjusting the threshold setting plane of the analog comparator (the thresholds of the images in Figure 5e−h are set to 10%, 20%, 30%, and 50% of the maximum gray value, respectively), when the pixel current is lower than the set threshold, its output is set to zero, thereby achieving denoising of the image to different degrees. The output images are then normalized and input into a neural network with a 784-neuron input layer, a 100-neuron hidden layer, and a 10-neuron output layer for image recognition. After 40 training epochs, the recognition accuracy of the MNIST dataset with noise is only about 55%, as shown in Figure 5e. When the threshold is greater than 30%, the recognition accuracy of both the ideal and denoised datasets becomes comparable, reaching approximately 93% after 40 training epochs, as shown in Figure 5f−h. This is a significant improvement compared to the recognition accuracy before preprocessing. The recognition accuracy improves as the degree of preprocessing increases. This demonstrates that the preprocessing process of NVSs can extract key information to enhance the accuracy of color image recognition.

https://doi.org/10.1021/acsami.5c09650
ACS Appl. Mater. Interfaces 2025, 17, 48465−48473

Scheme 1. Schematic of the Synthesis of the Au/CBB/FTO Devices

CONCLUSION

In summary, the biomimetic porous photoelectric synaptic device achieves conversion between STP and LTP by adjusting the incident light frequency. It simulates wavelength-regulated excitatory and inhibitory synaptic plasticity, and the underlying mechanism is inspired by the natural function of corals. This light-tunable synaptic plasticity enables effective color image recognition, and the results offer insights into the advancement of intelligent vision systems.

EXPERIMENTAL METHODS

Preparation of CBB Film. CBB PNCs were prepared by a supersaturated crystallization method. CsBr (Aladdin, 99.999%; 0.2 mmol) was mixed with $BiBr_3$ (Aladdin, 99.99%; 0.13 mmol) and dissolved in DMSO (Aladdin, 99.8%; 3 mL) and N-octylamine (Olam) (Aladdin, 99%; 33 μL) to produce a yellow clarified CBB perovskite precursor solution after stirring at room temperature for 12 h. The precursor solution was rapidly injected into a mixture containing 30 mL of ethanol and 3 mL of oleic acid (OA) (Aladdin, 99%) under vigorous stirring at 80 °C for 10 min to form CBB PNCs. Figure S12a shows the low-magnification transmission electron microscopy (TEM) image of the synthesized CBB PNCs. The CBB PNCs exhibited a quasi-spherical shape with an average diameter of 9.3 nm and a size distribution of ∼1.4 nm (Figure S12b). The HR-TEM images reveal an interlayer spacing of ∼0.33 nm, which can be indexed to the (003) crystal facet of the pure monodisperse CBB PNCs [Figure S12 c]. Figure S12d shows the Fast Fourier Transform (FFT) pattern of the nanocrystal, revealing a set of bright 6-fold symmetrical spots that can be indexed to the (100) and (002) planes, indicating highly crystalline CBB PNCs. After centrifugation at 12,000 rpm and drying in a vacuum oven (60 °C), the PNCs powder was placed in *n*-hexane and made into a solution with a concentration of 2 mg/mL. The centrifugal casting method was adopted to deposit the CBB film on the FTO substrate. The FTO glass (2×2 cm^2) was cleaned ultrasonically with acetone, ethanol, and deionized water successively. After drying with flowing N_2, the FTO glass was exposed to oxygen plasma for 15 min. It was then placed at the bottom of a centrifuge tube containing 10 mL of the nanocrystalline solution. After centrifugation at 6,000 rpm for 10 min, the sample was removed, and the solution was allowed to evaporate naturally.

Preparation of the Au/CBB/FTO Device. An Au (∼240 nm) top electrode was prepared on CBB/FTO by direct current (DC) magnetron sputtering. The electrode radius was 500 μm, the sputtering power was 80 W, the pressure was 6×10^{-4} Pa, and the Ar_2 flow rate was 30 sccm. The synthesis process is shown in Scheme 1

Characterization. The morphology and elemental composition of the samples were characterized by SEM (ZEISS Gemini SEM 300) and EDS mapping. The crystal structure of the CBB PNCs was examined by HR-TEM (JEM2100). The absorption spectra were acquired with a Shimadzu UV-3150 spectrophotometer. XPS and Raman scattering analyses were performed using the Esca Lab 250Xi and Nanofinder 30, respectively. The photoelectric measurements were carried out on the Keithley 4200-SCS parameter analyzer, AFG31000 Series Arbitrary Function Generator, and lasers with wavelengths of 405, 520, and 635 nm.

ASSOCIATED CONTENT

Supporting Information

The Supporting Information is available free of charge at https://pubs.acs.org/doi/10.1021/acsami.5c09650.

Cross-sectional EDS characterization of Au/CBB/FTO; optical bandgap characterization of CBB PNCs; *I*−*V* characteristic curves of the device at different wavelengths and different light intensities; EPSC characteristic; PPF characteristic; summary of key parameters for reported lead-free perovskite-based photoelectric synaptic devices; Summary of key parameters for reported lead-based perovskite-based photoelectric synaptic devices; SEM characterization of CBB PNCs film; EDS characterization of CBB PNCs film; XPS characterization of CBB PNCs film; E_g peak in the Raman spectra under dark and different illumination conditions; UPS characterization of CBB PNCs; energy band diagrams of device wavelength regulation mechanism; TEM characterization of CBB PNCs (PDF)

AUTHOR INFORMATION

Corresponding Authors

Qin Gao − *School of Applied Science, Beijing Information Science & Technology University, Beijing 102206, China*; Email: gaoqin@bistu.edu.cn

Anping Huang − *School of Physics, Beihang University, Beijing 100191, China*; orcid.org/0000-0002-1365-3575; Phone: 86-10-61716876; Email: aphuang@buaa.edu.cn; Fax: 86-10-61716876

Authors

Juan Gao − *School of Physics, Beihang University, Beijing 100191, China*

Jiangshun Huang − *School of Physics, Beihang University, Beijing 100191, China*

Xueli Geng − *School of Physics, Beihang University, Beijing 100191, China*

Pengzhan Li − *School of Physics, Beihang University, Beijing 100191, China*
Yihang Liu − *School of Physics, Beihang University, Beijing 100191, China*
Qiaofeng Yang − *School of Physics, Beihang University, Beijing 100191, China*
Hao Zhang − *School of Space and Earth Sciences, Beihang University, Beijing 100191, China*
Mei Wang − *School of Physics, Beihang University, Beijing 100191, China*
Zhisong Xiao − *School of Physics, Beihang University, Beijing 100191, China; School of Applied Science, Beijing Information Science & Technology University, Beijing 102206, China;* orcid.org/0000-0001-7309-9900
Paul K. Chu − *Department of Physics, Department of Materials Science and Engineering, and Department of Biomedical Engineering, City University of Hong Kong, Kowloon, Hong Kong 999077, China;* orcid.org/0000-0002-5581-4883
Ruifeng Lu − *Shanghai Institute of Satellite Engineering, Shanghai 201109, China*

Complete contact information is available at: https://pubs.acs.org/10.1021/acsami.5c09650

Notes

The authors declare no competing financial interest.

■ ACKNOWLEDGMENTS

This research was supported by the National Natural Science Foundation of China (Grant Nos. 52403315 and 52473251), the Industry University Research Cooperation Fund of the Eighth Research Institute of China Aerospace Science and Technology Corporation (SAST2023-030), the National Key Research and Development Program of China (Grant No. 2021YFB3900701), and the City University of Hong Kong Donation Research Grant (Grant Nos. DON-RMG 9229021 and 9220061).

■ REFERENCES

(1) Yang, Y.; Pan, C.; Li, Y.; Yangdong, X.; Wang, P.; Li, Z.-A.; Wang, S.; Yu, W.; Liu, G.; Cheng, B.; et al. In-sensor dynamic computing for intelligent machine vision. *Nat. Electron.* **2024**, *7* (3), 225−233.
(2) Tan, H.; van Dijken, S. Dynamic machine vision with retinomorphic photomemristor-reservoir computing. *Nat. Commun.* **2023**, *14* (1), 2169.
(3) Dodda, A.; Jayachandran, D.; Subbulakshmi Radhakrishnan, S.; Pannone, A.; Zhang, Y.; Trainor, N.; Redwing, J. M.; Das, S. Bioinspired and Low-Power 2D Machine Vision with Adaptive Machine Learning and Forgetting. *ACS Nano* **2022**, *16* (12), 20010−20020.
(4) Zhang, Z.; Wang, S.; Liu, C.; Xie, R.; Hu, W.; Zhou, P. All-in-one two-dimensional retinomorphic hardware device for motion detection and recognition. *Nat. Nanotechnol.* **2022**, *17* (1), 27−32.
(5) Long, Z.; Qiu, X.; Chan, C. L. J.; Sun, Z.; Yuan, Z.; Poddar, S.; Zhang, Y.; Ding, Y.; Gu, L.; Zhou, Y.; et al. A neuromorphic bionic eye with filter-free color vision using hemispherical perovskite nanowire array retina. *Nat. Commun.* **2023**, *14* (1), 1972.
(6) Zhu, S.; Xie, T.; Lv, Z.; Leng, Y.-B.; Zhang, Y.-Q.; Xu, R.; Qin, J.; Zhou, Y.; Roy, V. A. L.; Han, S.-T. Hierarchies in Visual Pathway: Functions and Inspired Artificial Vision. *Adv. Mater.* **2024**, *36* (6), 2301986.
(7) Liu, W.; Yang, X.; Wang, Z.; Li, Y.; Li, J.; Feng, Q.; Xie, X.; Xin, W.; Xu, H.; Liu, Y. Self-powered and broadband opto-sensor with bionic visual adaptation function based on multilayer γ-InSe flakes. *Light: Sci. Appl.* **2023**, *12* (1), 180.
(8) Shi, J.; Lin, Y.; Wang, Z.; Shan, X.; Tao, Y.; Zhao, X.; Xu, H.; Liu, Y. Adaptive Processing Enabled by Sodium Alginate Based Complementary Memristor for Neuromorphic Sensory System. *Adv. Mater.* **2024**, *36* (32), 2314156.
(9) Shi, L.; Shi, K.; Zhang, Z.-C.; Li, Y.; Wang, F.-D.; Si, S.-H.; Liu, Z.-B.; Lu, T.-B.; Chen, X.-D.; Zhang, J. Flexible retinomorphic vision sensors with scotopic and photopic adaptation for a fully flexible neuromorphic machine vision system. *SmartMater* **2024**, *5*, No. e1285.
(10) Shao, H.; Li, Y.; Yang, W.; He, X.; Wang, L.; Fu, J.; Fu, M.; Ling, H.; Gkoupidenis, P.; Yan, F.; et al. A Reconfigurable Optoelectronic Synaptic Transistor with Stable Zr-$CsPbI_3$ Nanocrystals for Visuomorphic Computing. *Adv. Mater.* **2023**, *35* (12), 2208497.
(11) Li, P.; Zhang, M.; Zhou, Q.; Zhang, Q.; Xie, D.; Li, G.; Liu, Z.; Wang, Z.; Guo, E.; He, M.; et al. Reconfigurable optoelectronic transistors for multimodal recognition. *Nat. Commun.* **2024**, *15* (1), 3257.
(12) Hu, L.; Yang, J.; Wang, J.; Cheng, P.; Chua, L. O.; Zhuge, F. All-Optically Controlled Memristor for Optoelectronic Neuromorphic Computing. *Adv. Funct. Mater.* **2021**, *31* (4), 2005582.
(13) Liang, J.; Yu, X.; Qiu, J.; Wang, M.; Cheng, C.; Huang, B.; Zhang, H.; Chen, R.; Pei, W.; Chen, H. All-Optically Controlled Artificial Synapses Based on Light-Induced Adsorption and Desorption for Neuromorphic Vision. *ACS Appl. Mater. Interfaces* **2023**, *15* (7), 9584−9592.
(14) Liao, F.; Zhou, Z.; Kim, B. J.; Chen, J.; Wang, J.; Wan, T.; Zhou, Y.; Hoang, A. T.; Wang, C.; Kang, J.; et al. Bioinspired in-sensor visual adaptation for accurate perception. *Nat. Electron.* **2022**, *5* (2), 84−91.
(15) Gao, C.; Liu, D.; Xu, C.; Bai, J.; Li, E.; Zhang, X.; Zhu, X.; Hu, Y.; Lin, Z.; Guo, T.; et al. Feedforward Photoadaptive Organic Neuromorphic Transistor with Mixed-Weight Plasticity for Augmenting Perception. *Adv. Funct. Mater.* **2024**, *34* (18), 2313217.
(16) Ge, S.; Huang, F.; He, J.; Xu, Z.; Sun, Z.; Han, X.; Wang, C.; Huang, L.-B.; Pan, C. Bidirectional Photoresponse in Perovskite-ZnO Heterostructure for Fully Optical-Controlled Artificial Synapse. *Adv. Opt. Mater.* **2022**, *10* (11), 2200409.
(17) Xie, D.; Wei, L.; Xie, M.; Jiang, L.; Yang, J.; He, J.; Jiang, J. Photoelectric Visual Adaptation Based on 0D-$CsPbBr_3$-Quantum-Dots/2D-MoS_2 Mixed-Dimensional Heterojunction Transistor. *Adv. Funct. Mater.* **2021**, *31* (14), 2010655.
(18) Wang, C.; Bian, Y.; Liu, K.; Qin, M.; Zhang, F.; Zhu, M.; Shi, W.; Shao, M.; Shang, S.; Hong, J.; et al. Strain-insensitive viscoelastic perovskite film for intrinsically stretchable neuromorphic vision-adaptive transistors. *Nat. Commun.* **2024**, *15* (1), 3123.
(19) Hong, S.; Choi, S. H.; Park, J.; Yoo, H.; Oh, J. Y.; Hwang, E.; Yoon, D. H.; Kim, S. Sensory Adaptation and Neuromorphic Phototransistors Based on $CsPb(Br_{1-x}I_x)_3$ Perovskite and MoS_2 Hybrid Structure. *ACS Nano* **2020**, *14* (8), 9796−9806.
(20) Cao, F.; Hu, Z.; Yan, T.; Hong, E.; Deng, X.; Wu, L.; Fang, X. A Dual-Functional Perovskite-Based Photodetector and Memristor for Visual Memory. *Adv. Funct. Mater.* **2023**, *35* (44), 2304550.
(21) Zhao, W.; Lin, Z.; Chen, H.; Xu, S.; Chen, E.; Guo, T.; Ye, Y.; Chen, H. Perovskite-Doped Modulated Color-Selective Photosynaptic Transistors for Target Object Recognition. *Nano Lett.* **2024**, *24* (32), 9937−9945.
(22) Wei, H.; Yao, G.; Ni, Y.; Yang, L.; Liu, J.; Sun, L.; Zhang, X.; Yang, J.; Xiao, Y.; Zheng, F.; et al. Flexible Electro-Optical Perovskite/Electrolyte Synaptic Transistor to Emulate Photoelectric-Synergistic Neural Learning Rules and Reflex-Arc Behavior. *Adv. Funct. Mater.* **2023**, *33* (46), 2304000.
(23) Gong, G.; Zhou, Y.; Xiong, Z.; Sun, T.; Li, H.; Li, Q.; Zhao, W.; Zhang, G.; Zhai, Y.; Lv, Z.; et al. An Antagonistic Photovoltaic Memristor for Bioinspired Active Contrast Adaptation. *Adv. Funct. Mater.* **2024**, *36* (50), 2409844.

(24) Kramer, N.; Tamir, R.; Ben-Zvi, O.; Jacques, S. L.; Loya, Y.; Wangpraseurt, D. Efficient light-harvesting of mesophotic corals is facilitated by coral optical traits. *Funct. Ecol.* **2022**, *36* (2), 406−418.
(25) Smith, E. G.; D'Angelo, C.; Sharon, Y.; Tchernov, D.; Wiedenmann, J. Acclimatization of symbiotic corals to mesophotic light environments through wavelength transformation by fluorescent protein pigments. *Proc. R. Soc. B* **2017**, *284* (1858), 20170320.
(26) Mi, Y.; Li, Y.; Tao, Y.; Chen, Y.; Bai, J.; Wang, G.; Wang, L.; Ma, S.; Wang, B. Advanced bionic inverted coral solar evaporator: Enhancing sustainable water utilization with efficient and salt-resistant evaporation. *Chem. Eng. J.* **2024**, *496*, 153890.
(27) Li, J.; Zhang, Y.; Yao, C.; Qin, N.; Chen, R.; Bao, D. Optoelectronic Modulation of Interfacial Defects in Lead-Free Perovskite Films for Resistive Switching. *Adv. Electron. Mater.* **2022**, *8* (4), 2101094.
(28) Lv, Y.; Chen, S.; Chen, J.; Li, W.; Li, W.; An, Y.; Fu, Y.; Mai, W.; Zhao, C. lead-Free Perovskite Photodetectors for Fast Fourier Single-Detector Imaging. *ACS Photonics* **2024**, *11* (9), 3621−3629.
(29) Kim, S.-Y.; Park, D.-A.; Park, N.-G. Synthetic Powder-Based Thin (<0.1 μm) $Cs_3Bi_2Br_9$ Perovskite Films for Air-Stable and Viable Resistive Switching Memory. *ACS Appl. Electron. Mater.* **2022**, *4* (5), 2388−2395.
(30) Biswas, A.; Rowberg, A. J. E.; Yadav, P.; Moon, K.; Blanchard, G. J.; Kweon, K. E.; Kim, S. Ag Intercalation in Layered $Cs_3Bi_2Br_9$ Perovskite for Enhanced Light Emission with Bound Interlayer Excitons. *J. Am. Chem. Soc.* **2024**, *146* (29), 19919−19928.
(31) Wang, T.; Xin, S.; Liu, Y.; Ji, Z.; Liu, G.; Zhang, S.; Wang, T.; Wang, F.; Teng, B.; Ji, S. Fast ultraviolet detection response achieved in high-quality $Cs_3Bi_2Br_9$ single crystals grown by an improved anti-solvent method. *J. Mater. Chem. C* **2024**, *12* (16), 5934−5940.
(32) Gou, R.; Shi, C.; Zhou, S.; Huang, Z.; Ouyang, Z.; He, S.; Zhao, J.; Xiao, Y.; Lei, S.; Cheng, B. Self-Powered Photodetector Based on Ag/$CH_3NH_3PbI_3$/C Asymmetric Dual-Terminal Device. *ACS Appl. Mater. Interfaces* **2023**, *15* (47), 54863−54874.
(33) Gao, Q.; Huang, A.; Hu, Q.; Zhang, X.; Chi, Y.; Li, R.; Ji, Y.; Chen, X.; Zhao, R.; Wang, M.; et al. Stability and Repeatability of a Karst-like Hierarchical Porous Silicon Oxide-Based Memristor. *ACS Appl. Mater. Interfaces* **2019**, *11* (24), 21734−21740.
(34) Lin, L.; Yang, L.; Du, G.; Li, X.; Li, Y.; Deng, J.; Wei, K.; Zhang, J. Light Soaking Effects in Perovskite Solar Cells: Mechanism, Impacts, and Elimination. *ACS Appl. Energy Mater.* **2023**, *6* (20), 10303−10318.
(35) Wang, F.; Zhang, T.; Xie, R.; Wang, Z.; Hu, W. How to characterize figures of merit of two-dimensional photodetectors. *Nat. Commun.* **2023**, *14* (1), 2224.
(36) Wen, X.; Fu, J.; Zhang, X.; Meng, X.; Tian, Y.; Li, J.; Yu, G.; Hao, Y.; Zhu, Y. Achieving Immune Activation by Suppressing the IDO1 Checkpoint with Sono-Targeted Biobromination for Antitumor Combination Immunotherapy. *J. Am. Chem. Soc.* **2024**, *146* (35), 24580−24590.
(37) Li, B.; Lin, M.; Kan, C.; Hang, P.; Yao, Y.; Hu, Z.; Wang, Y.; Zhang, Y.; Zhong, W.; Yang, D.; et al. Revealing the Correlation of Light Soaking Effect with Ion Migration in Perovskite Solar Cells. *Sol. RRL* **2022**, *6* (7), 2200050.
(38) Chen, X.; Zhou, J.; Luo, J.; Zhang, J.; Qiu, P.; Shi, X. Ultralow Thermal Conductivity in Vacancy-Ordered Halide Perovskite $Cs_3Bi_2Br_9$ with Strong Anharmonicity and Wave-Like Tunneling of Low-Energy Phonons. *Small* **2024**, *20* (46), 2405276.
(39) Samanta, D.; Mazumder, A.; Chaudhary, S. P.; Ghosh, B.; Saha, P.; Bhattacharyya, S.; Mukherjee, G. D. Phonon anharmonicity and soft-phonon mediated structural phase transition in $Cs_3Bi_2Br_9$. *Phys. Rev. B* **2023**, *108* (5), 054104.
(40) Ren, Q.; He, Y.; Wang, H.; Sun, Y.; Dong, F. Rapid Energy Exchange between In Situ Formed Bromine Vacancies and CO_2 Molecules Enhances CO_2 Photoreduction. *Research* **2023**, *6*, 0244.
(41) Jeon, S.; Ahn, S.-E.; Song, I.; Kim, C. J.; Chung, U. I.; Lee, E.; Yoo, I.; Nathan, A.; Lee, S.; Ghaffarzadeh, K.; et al. Gated three-terminal device architecture to eliminate persistent photoconductivity in oxide semiconductor photosensor arrays. *Nat. Mater.* **2012**, *11* (4), 301−305.
(42) Yang, J.; Hu, L.; Shen, L.; Wang, J.; Cheng, P.; Lu, H.; Zhuge, F.; Ye, Z. Optically driven intelligent computing with ZnO memristor. *Fundam. Res.* **2024**, *4* (1), 158−166.
(43) Zhang, G.; Wei, Q.; Ghasemi, M.; Liu, G.; Wang, J.; Zhou, B.; Luo, J.; Yang, Y.; Jia, B.; Wen, X. Positive and Negative Effects under Light Illumination in Halide Perovskites. *Small Sci.* **2024**, *4* (7), 2400028.
(44) Phung, N.; Mattoni, A.; Smith, J. A.; Skroblin, D.; Köbler, H.; Choubrac, L.; Breternitz, J.; Li, J.; Unold, T.; Schorr, S.; Gollwitzer, C.; et al. Photoprotection in metal halide perovskites by ionic defect formation. *Joule* **2022**, *6* (9), 2152−2174.
(45) Liu, Z.; Zhang, M.; Zhang, Q.; Li, G.; Xie, D.; Wang, Z.; Xie, J.; Guo, E.; He, M.; Wang, C.; et al. All-In-One Optoelectronic Transistors for Bio-Inspired Visual System. *Adv. Mater.* **2024**, *36* (48), 2409520.
(46) Wang, Y.; Wang, F.; Wang, Z.; Wang, J.; Yang, J.; Yao, Y.; Li, N.; Sendeku, M. G.; Zhan, X.; Shan, C.; et al. Reconfigurable photovoltaic effect for optoelectronic artificial synapse based on ferroelectric p−n junction. *Nano Res.* **2021**, *14* (11), 4328−4335.
(47) Wei, B.; Chen, Y.; Han, X.; Kang, Y.; Liang, B.; Li, C.; Yang, X.; Fang, L.; Peng, Y. Ultra-low Power MoS_2 Optoelectronic Synapse with Wavelength Sensitivity for Color Target Recognition. *Sci. China Inf. Sci.* **2025**, *68* (4), 140406.
(48) Luo, X.; Chen, C.; He, Z.; Wang, M.; Pan, K.; Dong, X.; Li, Z.; Liu, B.; Zhang, Z.; Wu, Y.; et al. A bionic self-driven retinomorphic eye with ionogel photosynaptic retina. *Nat. Commun.* **2024**, *15* (1), 3086.

https://doi.org/10.1021/acsami.5c09650
ACS Appl. Mater. Interfaces 2025, 17, 48465−48473

Supporting Information

Multiwavelength-Responsive Plasticity in a Bias-Free Perovskite Synaptic Device for Neuromorphic Vision

Juan Gao[1], Qin Gao[2], Jiangshun Huang[1], Xueli Geng[1], Pengzhan Li[1], Yihang Liu[1], Qiaofeng Yang[1], Hao Zhang[3], Mei Wang[1], Zhisong Xiao[1&2], Paul K. Chu[4], Ruifeng Lu[5], Anping Huang[1]**

[1] *School of Physics, Beihang University, Beijing 100191, China*

[2] *School of Applied Science, Beijing Information Science & Technology University, Beijing 102206, China*

[3] *School of Space and Earth Sciences, Beihang University, Beijing 100191, China*

[4] *Department of Physics, Department of Materials Science and Engineering, and Department of Biomedical Engineering, City University of Hong Kong, Tat Chee Avenue, Kowloon, Hong Kong, China*

[5] *Shanghai Institute of Satellite Engineering, Shanghai 201109, China*

* *Corresponding Authors*

gaoqin@bistu.edu.cn; aphuang@buaa.edu.cn; Tel: 86-10-61716876; Fax: 86-10-61716876*

Table of contents

1. Cross-sectional EDS characterization of Au/CBB/FTO

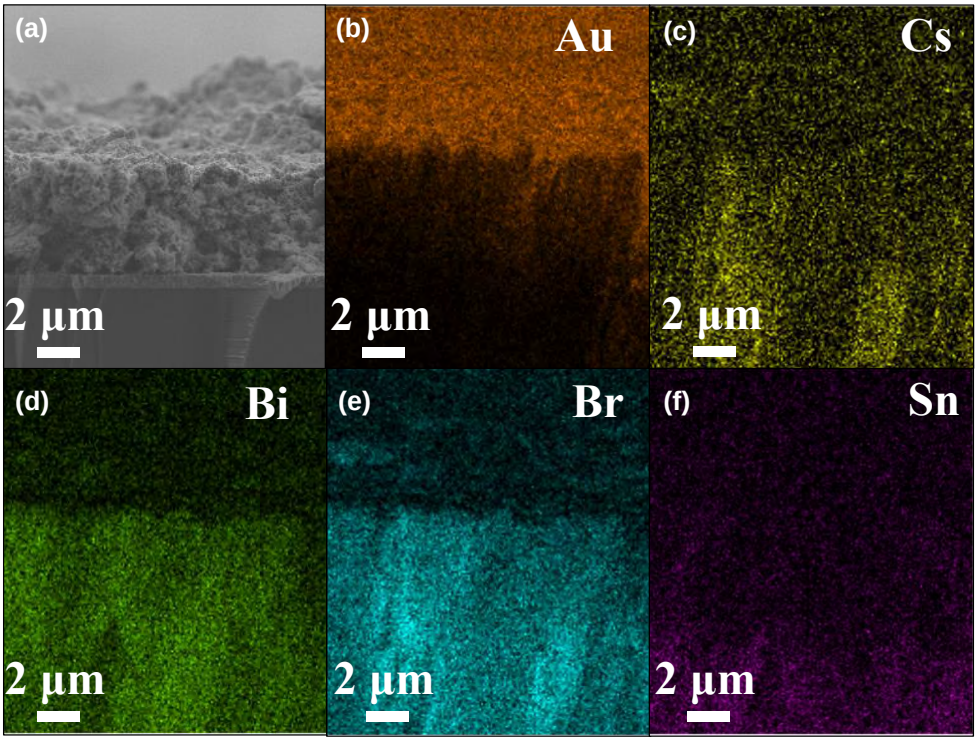

Figure S1. Cross-sectional EDS images of Au/CBB/FTO.

2. Optical bandgap characterization of CBB PNCs

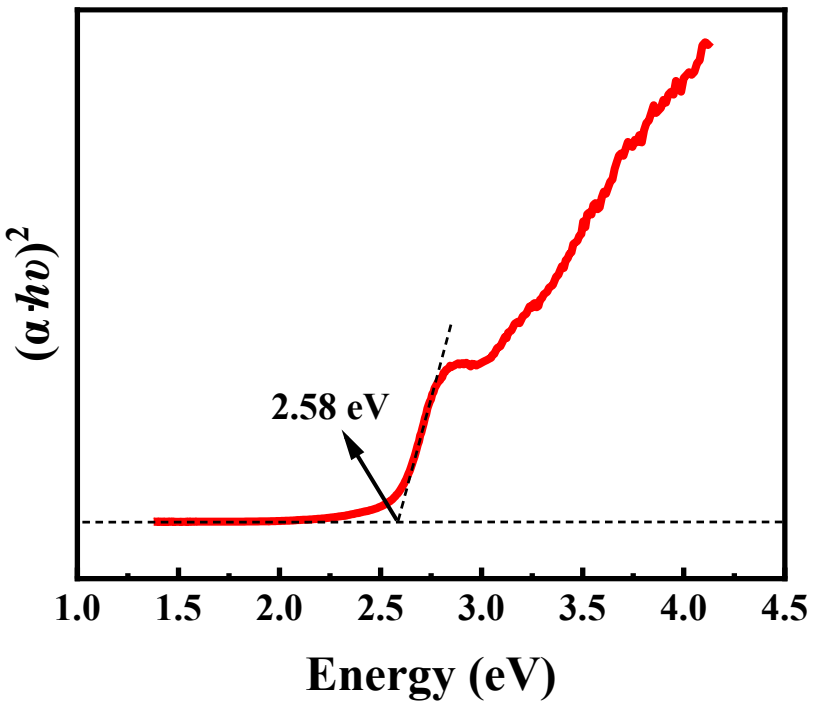

Figure S2. Calculation of the optical bandgap of CBB PNCs using the Tauc method.

The bandgap of CBB PNCs (direct bandgap) is estimated using Tauc equation[1]:

$$(\alpha \cdot h\nu)^2 = \mathrm{A}(h\nu - E_g) \quad (1)$$

in which α is the absorption coefficient, h is Planck's constant, ν is the frequency, A is a constant, E_g is the bandgap. The direct bandgap of the as-grown CBB PNCs is estimated to be around 2.58 eV.

3. *I-V* characteristic curves of the device at different wavelengths and different light intensities

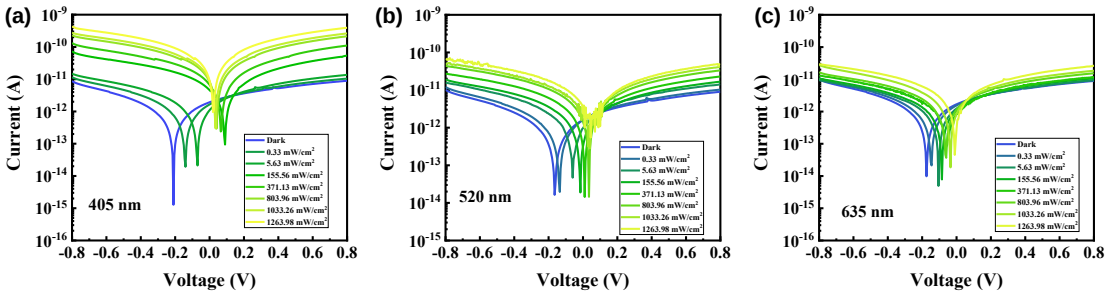

Figure S3. *I-V* characteristic curves of different light intensities at different wavelengths: (a) 405 nm; (b) 520 nm; (c) 635 nm.

4. EPSC characteristic

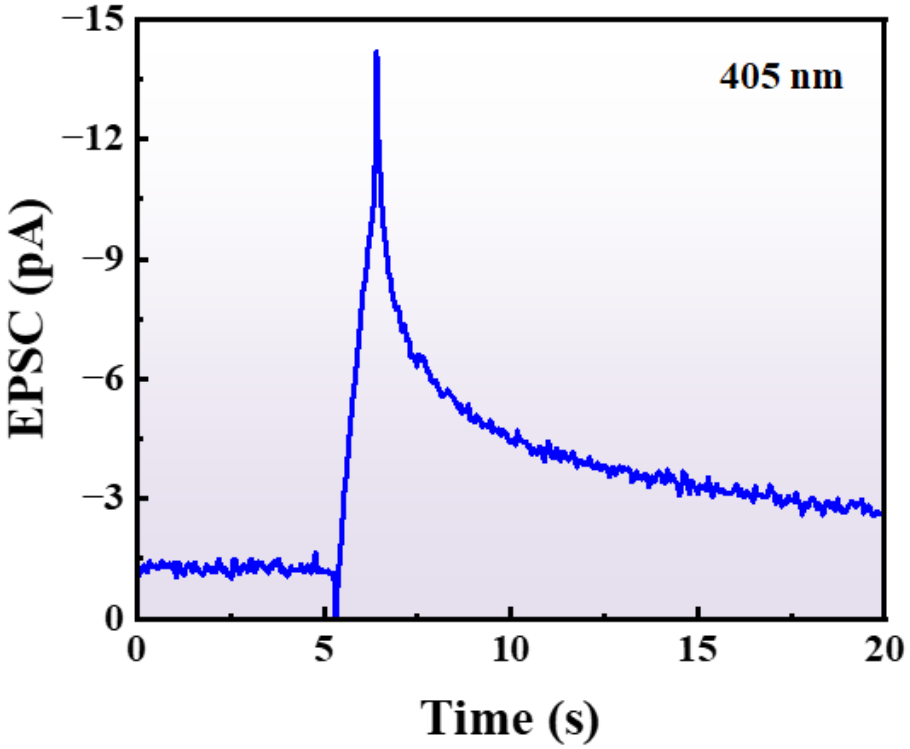

Figure S4. EPSC is triggered by a light pulse with a wavelength of 405 nm, a power density of 0.8×10^{-3} mW/cm^2, and a width of 1 s.

EPSC triggered by the light pulse with power density of 0.8×10^{-3} mW/cm^2 and a width of 1 s. The energy consumption of the device is calculated according to the relationship formula[2]: $E=P\times S\times t_{light}$, where P is the light power density, S is the photosensitive area of device, t_{light} is light pulse width. The energy consumption is 6.8 nJ.

5. PPF characteristic

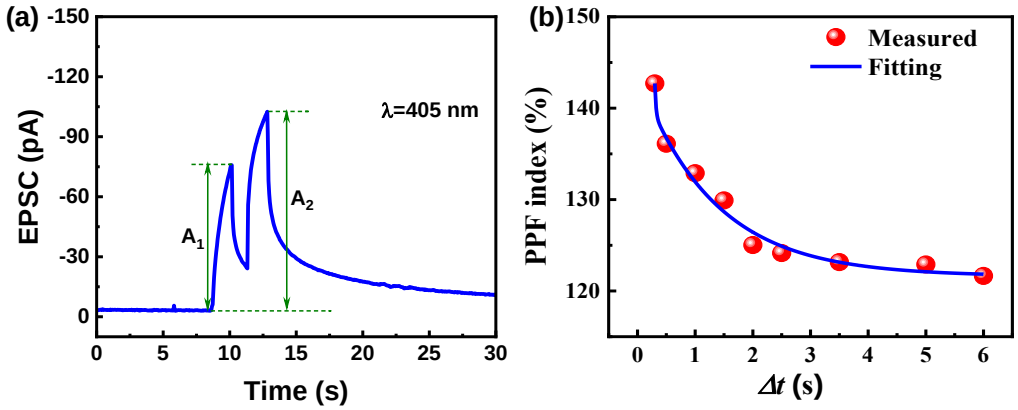

Figure S5. (a) Light pulse pair with a 1 s interval and light intensity of 156 mW cm^{-2} at 405 nm; (b) PPF index as a function of light spike interval time, Δt. The PPF index is defined as the ratio of A_2/A_1, where A_2 and A_1 represent the EPSC by the second and the first light pulses, respectively.

6. Summary of key parameters for reported lead-free perovskite-based photoelectric synaptic devices

Table S1. Properties of lead-free perovskite-based photoelectric synaptic devices.

Materials	**Device type**	**λ （nm）**	**Stimulus signal**	**PPF index**	**Energy consumption**	**Ref.**
PEA_2SnI_4/Y6	Three-terminal	450-808	Electric, light	160%	/	[3]
$Cs_3Bi_2I_9$/DPPDTT	Three-terminal	405, 532, 635	Electric, light	123%	/	[4]
$Cs_3Bi_2Br_9$	Two-terminal	445, 520, 660	Light	183%	0	[5]
$Cs_2AgBiBr_6$	Two-terminal	532,660	Electric, light	/	0.4-1 nJ	[6]
$(PEA)_2SnI_4$	Three-terminal	460-630	Electric, light	129.7%	/	[7]
$Cs_3Bi_2Br_9$ PNCs	**Two-terminal**	**405, 520, 635**	**Light**	142.7%	**6.8 nJ**	**Our work**

7. Summary of key parameters for reported lead-based perovskite-based photoelectric synaptic devices

Table S2. Properties of lead-based perovskite photoelectric synaptic devices.

Materials	Device type	λ (nm)	Stimulus signal	PPF index	Energy consumption	Ref.
$CsPbBr_3$/P3HT	Three-terminal	445	Electric, light	179%	/	[8]
$MAPbBr_3$/ZnO	Two-terminal	365	light	/	17.1 μJ	[9]
$CsPbBr_3/MoS_2$	Three-terminal	360	Electric, light	/	/	[10]
$CsPb(Br_{1-x}I_x)_3/MoS_2$	Three-terminal	405	light	/	/	[11]
$CsPbBr_3$/PDPP-TT	Three-terminal	365	Electric, light	133%	/	[12]
$CsPbBr_3$/pentacene	Three-terminal	400-1050	Electric, light	/	/	[13]

BCP/$MAPbBr_3$	Three-terminal	405,530	Electric, light	160%	5.8 pJ	[14]
$CsPb_{0.5}Sn_{0.5}Br_3$	Three-terminal	405-532	Electric, light	109%	0.1 fJ	[15]
Zr-$CsPbI_3$/ pentacene	Three-terminal	405,650	Electric, light	/	/	[16]
$Cs_3Bi_2Br_9$ PNCs	**Two-terminal**	**405, 520, 635**	**Light**	142.7%	**6.8 nJ**	**Our work**

8. SEM characterization of CBB PNCs film

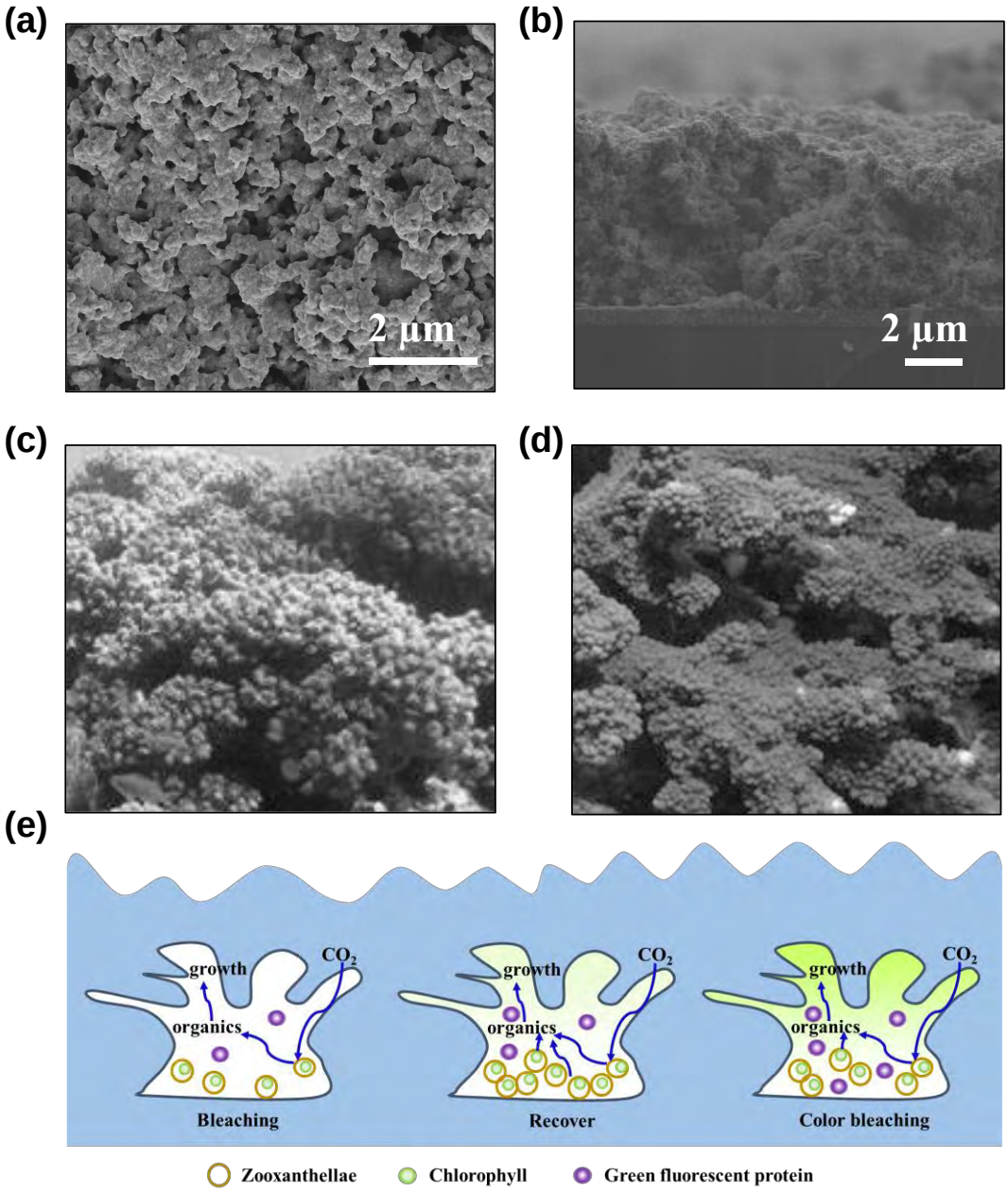

Figure S6. SEM images of (a) Surface and (b) Cross-section of the CBB film; (c, d) Natural coral structure from different perspectives in nature; (e) Schematic illustration of light enhancement effects in natural corals.

9. EDS characterization of CBB PNCs film

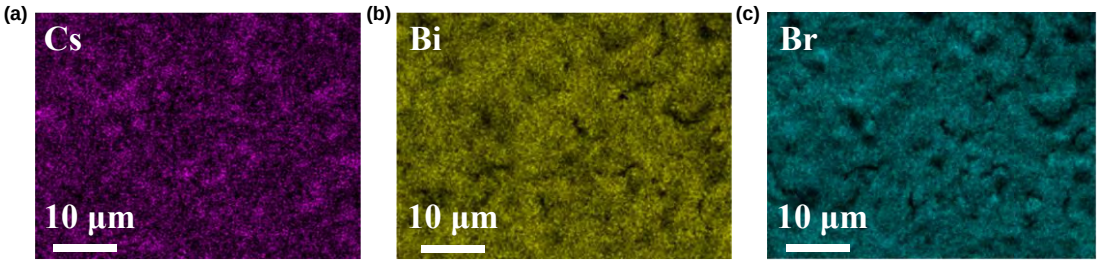

Figure S7. EDS elemental maps of the CBB PNCs film (a) Cs; (b) Bi; (c) Br.

10. XPS characterization of CBB PNCs film

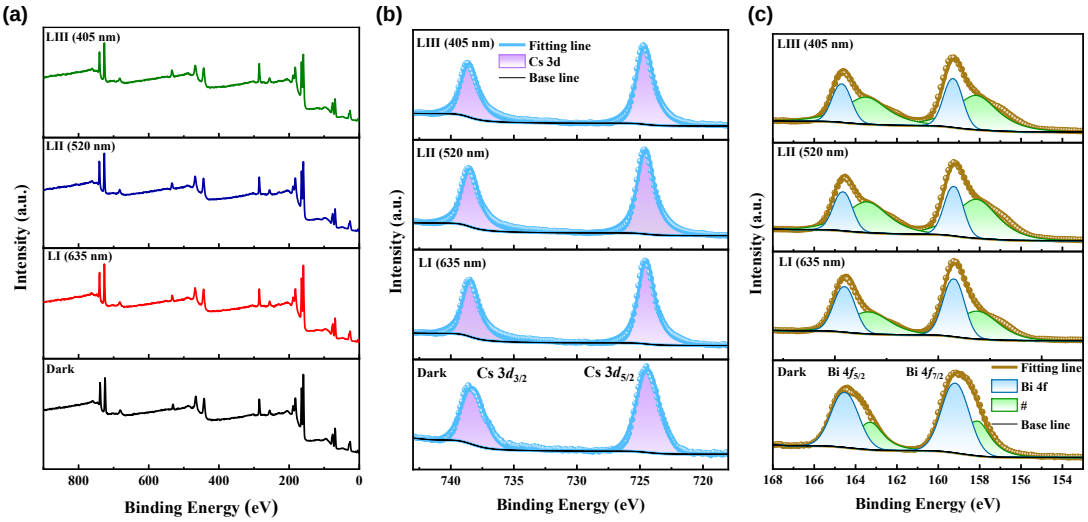

Figure S8. XPS spectra of the CBB PNCs film: (a) Survey; (b) Cs 3*d*; (c) Bi 4*f*.

11. E_g peak in the Raman spectra under dark and different illumination conditions

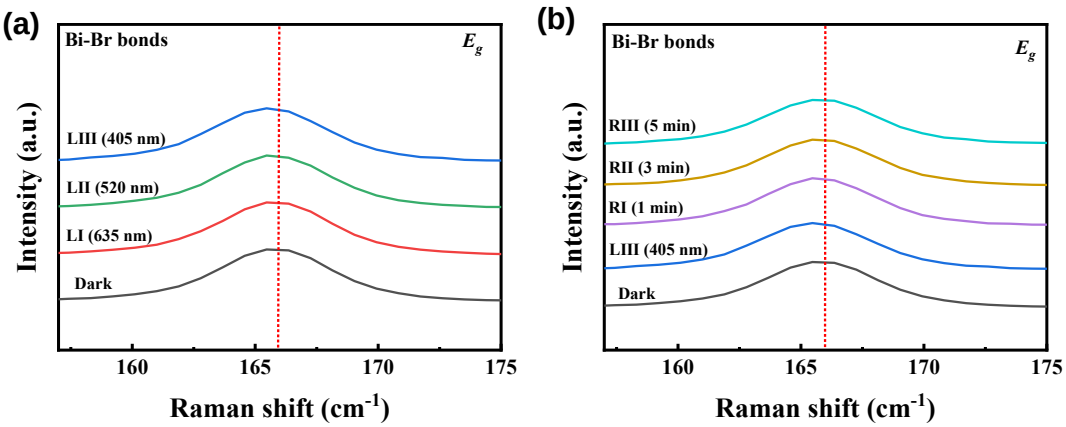

Figure S9. (a) E_g displacement in Raman spectra under different light conditions; (b) E_g displacement in Raman spectra with different recovery times after illumination.

12. UPS characterization of CBB PNCs

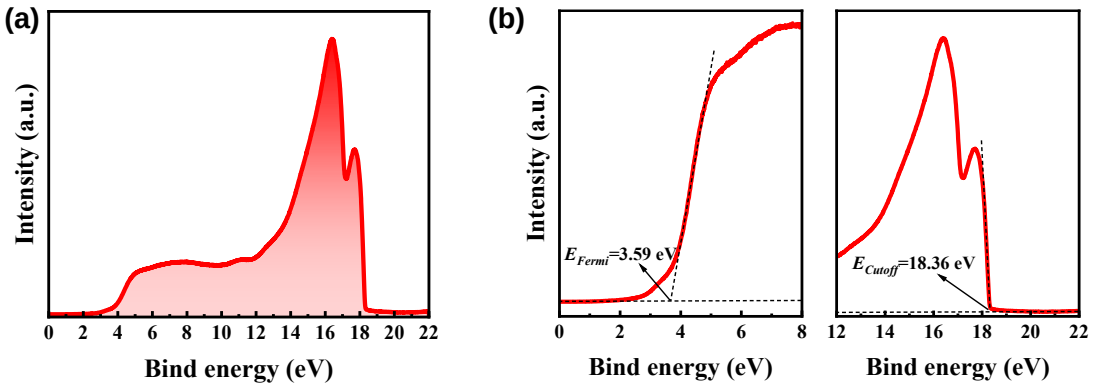

Figure S10. (a) UPS spectrum of the CBB PNCs; (b) Enlarged view of the low- and high-binding-energy regions of the spectrum.

UPS measurements is performed to determine the valence band maximum of CBB PNCs, and the value can be obtained by the following formulas[17]:

$$E_{VBM} = h\nu - E_{cutoff} + E_{fermi} \quad (2)$$

$$E_{CBM} = E_{VBM} + E_g \quad (3)$$

where $h\nu$ is the ultraviolet radiation energy (21.22 eV), E_{cutoff} is the binding energy of the secondary cutoffs in the spectra, and E_{Fermi} is the difference between the valence band maximum (E_{VBM}) and the Fermi level. Combining the bandgap energy of 2.58 eV, E_{VBM} and conduction band minimum (E_{CBM}) are 6.43 eV and 3.86 eV, respectively.

13. Energy band diagrams of device wavelength regulation mechanism

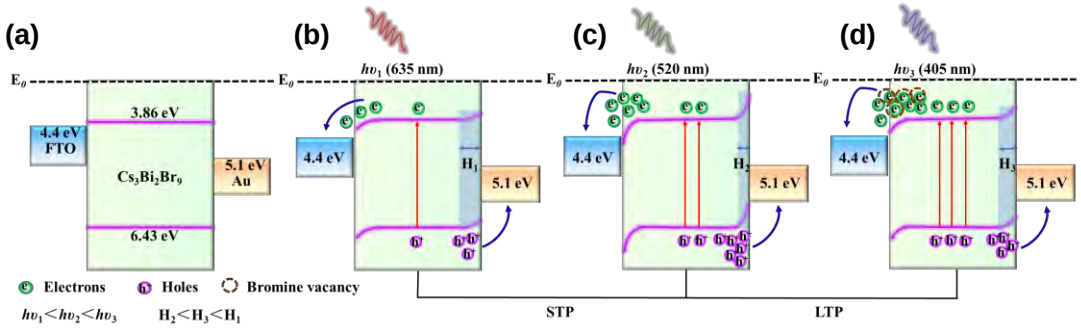

Figure S11. Schematic diagram of the energy band alignment: (a) Initial state, (b) 635 nm, (c) 520 nm, and (d) 405 nm.

14. TEM characterization of CBB PNCs

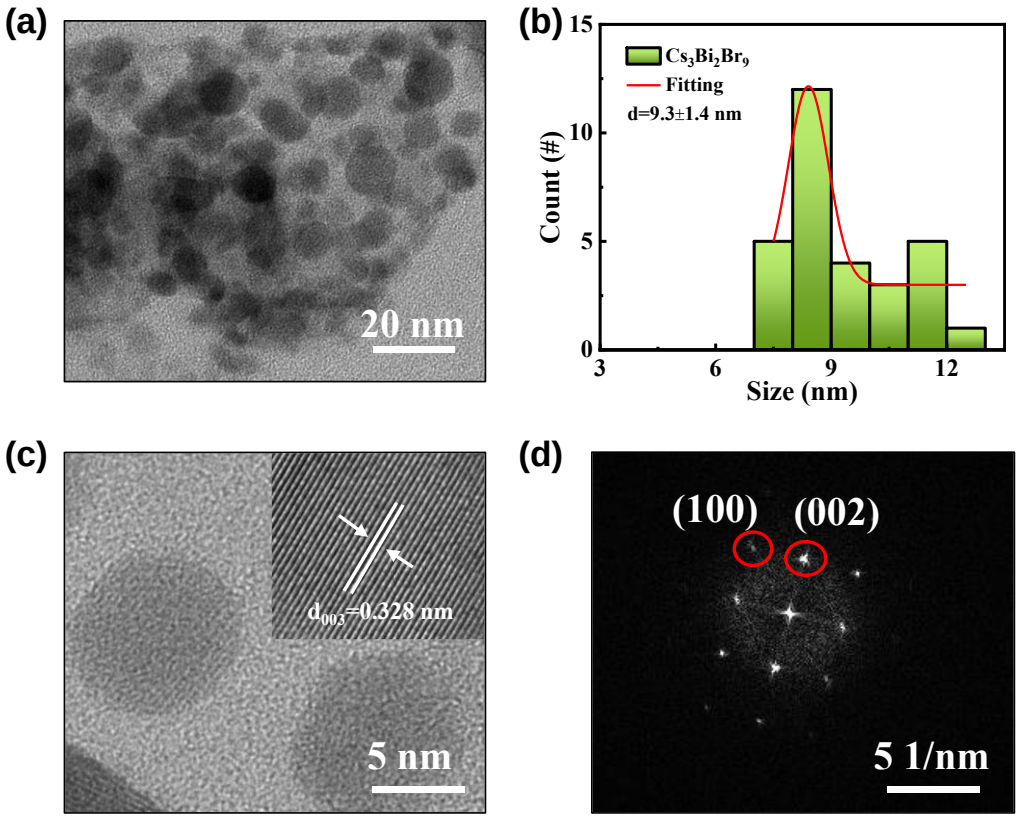

Figure S12. (a) TEM image of quasi-spherical CBB PNCs; (b) Size of CBB PNCs calculated by the Nano-Measure Particle Size Statistics software; (c) HR-TEM image of quasi-spherical CBB PNCs; (d) FFT pattern of CBB PNCs.

References

[1] Alshogeathri, S.; Cao, D.; Kim, D.; Yang, G. Gel growth and characterization of $Cs_3Bi_2Br_9$ perovskite single crystals for radiation detection. *Front. Phys.* **2023**, *11*, 1129301 DOI: 10.3389/fphy.2023.1129301

[2] Ji, Y.; Meng, Y.; Geng, X.; Sun, J.; Gao, Q.; Yin, H.; Gao, J.; Wang, R.; Wang, M.; Xiao, Z., et al. Retina-Inspired Flexible Visual Synaptic Device for Dynamic Image Processing. *ACS Appl. Mater. Interfaces*. **2025**, *17*(5), 7948-7957 DOI: 10.1021/acsami.4c16378

[3] Huang, X.; Li, Q.; Shi, W.; Liu, K.; Zhang, Y.; Liu, Y.; Wei, X.; Zhao, Z.; Guo, Y.; Liu, Y. Dual-Mode Learning of Ambipolar Synaptic Phototransistor Based on 2D Perovskite/Organic Heterojunction for Flexible Color Recognizable Visual System. *Small*. **2021**, *17*(36), 2102820 DOI: 10.1002/smll.202102820

[4] Li, Y.; Wang, J.; Yang, Q.; Shen, G. Flexible Artificial Optoelectronic Synapse based on Lead-Free Metal Halide Nanocrystals for Neuromorphic Computing and Color Recognition. *Adv. Sci.* **2022**, *9*(22), 2202123 DOI: 10.1002/advs.202202123

[5] Zhao, P.; Cui, M.; Li, Y.; Lao, J.; Jiang, C.; Luo, C.; Tian, B.; Lin, H.; Peng, H.; Duan, C.-G. Self-powered optoelectronic artificial synapses based on a lead-free perovskite film for artificial visual perception systems. *J. Mater. Chem. C*. **2023**, *11*(18), 6212-6219 DOI: 10.1039/D3TC00583F

[6] Sun, Q.; Guo, Z.; Zhu, X.; Jiang, Q.; Liu, H.; Liu, X.; Sun, C.; Zhang, Y.; Wu, L.; Li, R.-W. Optogenetics-inspired manipulation of synaptic memory using all-

optically controlled memristors. *Nanoscale*. **2023**, *15*(23), 10050-10056 DOI: 10.1039/D3NR00900A

[7] Sun, Y.; Qian, L.; Xie, D.; Lin, Y.; Sun, M.; Li, W.; Ding, L.; Ren, T.; Palacios, T. Photoelectric Synaptic Plasticity Realized by 2D Perovskite. *Adv. Funct. Mater.* **2019**, *29*(28), 1902538 DOI: 10.1002/adfm.201902538

[8] Gupta, G. K.; Kim, I.-J.; Park, Y.; Kim, M.-K.; Lee, J.-S. Inorganic Perovskite Quantum Dot-Mediated Photonic Multimodal Synapse. *ACS Appl. Mater. Interfaces.* **2023**, *15*(14), 18055-18064 DOI: 10.1021/acsami.2c23218

[9] Ge, S.; Huang, F.; He, J.; Xu, Z.; Sun, Z.; Han, X.; Wang, C.; Huang, L.-B.; Pan, C. Bidirectional Photoresponse in Perovskite-ZnO Heterostructure for Fully Optical-Controlled Artificial Synapse. *Adv. Opt. Mater.* **2022**, *10*(11), 2200409 DOI: 10.1002/adom.202200409

[10] Xie, D.; Wei, L.; Xie, M.; Jiang, L.; Yang, J.; He, J.; Jiang, J. Photoelectric Visual Adaptation Based on 0D-$CsPbBr_3$-Quantum-Dots/2D-MoS_2 Mixed-Dimensional Heterojunction Transistor. *Adv. Funct. Mater.* **2021**, *31*(14), 2010655 DOI: 10.1002/adfm.202304000

[11] Hong, S.; Choi, S. H.; Park, J.; Yoo, H.; Oh, J. Y.; Hwang, E.; Yoon, D. H.; Kim, S. Sensory Adaptation and Neuromorphic Phototransistors Based on $CsPb(Br_{1-x}I_x)_3$ Perovskite and MoS_2 Hybrid Structure. *ACS Nano*. **2020**, *14*(8), 9796-9806 DOI: 10.1021/acsnano.0c01689

[12] Kuang, J.; Liu, K.; Liu, M.; Shao, M.; Zhu, M.; Liu, G.; Wen, W.; Chen, J.; Qin, M.; Pan, Z., et al. Interface Defects Tuning in Polymer-Perovskite Phototransistors

for Visual Synapse and Adaptation Functions. *Adv. Funct. Mater.* **2023**, *33*(5), 2209502 DOI: 10.1002/adfm.202209502

[13] Moon, B. J.; Song, Y.-S.; Son, D.; Yang, H. Y.; Bae, S.; Lee, S.-K.; Lee, S. H.; Kim, T.-W. Implementation of Photosynaptic and Electrical Memory Functions in Organic Nano-Floating-Gate Transistors via a Perovskite-Nanocrystal-Based Nanocomposite Tunneling Layer. *Small Sci.* **2023**, *3*(9), 2300068 DOI: 10.1002/smsc.202300068

[14] Lee, K.; Han, H.; Kim, Y.; Park, J.; Jang, S.; Lee, H.; Lee, S. W.; Kim, H.; Kim, Y.; Kim, T., et al. Retina-Inspired Structurally Tunable Synaptic Perovskite Nanocones. *Adv. Funct. Mater.* **2021**, *31*(52), 2105596 DOI: 10.1002/adfm.202105596

[15] Zhang, J.; Liu, J.; Geng, H.; Wang, W.; Wei, Y.; Chen, M.; Kang, J.; Zhao, J. Low Power Consumption $CsPb_{0.5}Sn_{0.5}Br_3$ Quantum Dot-Based Photoelectric Synaptic Transistors for Neuromorphic Computing. *ACS Appl. Nano Mater.* **2025**, DOI: 10.1021/acsanm.5c02604

[16] Shao, H.; Li, Y.; Yang, W.; He, X.; Wang, L.; Fu, J.; Fu, M.; Ling, H.; Gkoupidenis, P.; Yan, F., et al. A Reconfigurable Optoelectronic Synaptic Transistor with Stable Zr-$CsPbI_3$ Nanocrystals for Visuomorphic Computing. *Adv. Mater.* **2023**, *35*(12), 2208497 DOI: 10.1002/adma.202208497

[17] Wang, J.; Li, Y.; Ma, L.; Shen, G.; Yang, Q. Air-Stabilized Lead-Free Hexagonal $Cs_3Bi_2I_9$ Nanocrystals for Ultrahigh-Performance Optical Detection. *Adv. Funct. Mater.* **2022**, *32*(30), 2203072 DOI: 10.1002/adfm.202203072